1   **Revision 1**

2

3   **Yakubovichite, $CaNi_2Fe^{3+}(PO_4)_3$, a new nickel phosphate mineral of non-meteoritic origin**

4

5   Sergey N. Britvin[1,2]*, Mikhail N. Murashko[1], Maria G. Krzhizhanovskaya[1], Yevgeny Vapnik[3],

6   Natalia S. Vlasenko[4], Oleg S. Vereshchagin[1], Dmitrii V. Pankin[5], Anatoly N. Zaitsev[1], and Anatoly A.

7   Zolotarev[1]

8

9   [1]Institute of Earth Sciences, Saint-Petersburg State University, Universitetskaya Nab. 7/9, St.

10   Petersburg, 199034, Russia.

11   [2]Nanomaterials Research Center, Kola Science Center, Russian Academy of Sciences, Fersman Str.

12   14, Apatity, 184200, Russia.

13   [3]Department of Geological and Environmental Sciences, Ben-Gurion University of the Negev, POB

14   653, Beer-Sheva, 84105, Israel.

15   [4]Geomodel Resource Center, Saint-Petersburg State University, Ulyanovskaya Str. 1, St. Petersburg,

16   198504, Russia.

17   [5]Center for Optical and Laser Materials Research, St. Petersburg State University, Ulyanovskaya

18   Str. 5, St. Petersburg, 199034, Russia

19

20

21   * Corresponding author. E-mail: sergei.britvin@spbu.ru

22

Abstract

23

24 Yakubovichite, $CaNi_2Fe^{3+}(PO_4)_3$, a new mineral containing up to 20 wt.% NiO, represents a novel

25 type of terrestrial phosphate mineralisation featuring an extreme enrichment in Ni. The mineral was

26 discovered in the Hatrurim Formation (Mottled Zone) – pyrometamorphic complex whose outcrops

27 are exposed in Israel and Jordan in the area coincident with the Dead Sea Transform fault system.

28 Nickel-rich minerals in these assemblages also include Ni phosphides: halamishite Ni_5P_4, negevite

29 NiP_2, transjordanite and orishchinite – two polymorphs of Ni_2P, nazarovite $Ni_{12}P_5$, polekovskyite

30 $MoNiP_2$; Ni-spinel trevorite $NiFe_2O_4$, bunsenite NiO, and nickeliferous members of the hematite-

31 eskolaite series, Fe_2O_3-Cr_2O_3 containing up to 2 wt.% NiO. Yakubovichite forms polycrystalline

32 segregations up to 0.2 mm in size composed of equant crystal grains, in association with

33 crocobelonite, hematite, other phosphates and phosphides. It has a deep yellow to lemon-yellow

34 colour; transparent to translucent with vitreous luster, with no cleavage. Mohs hardness = 4.

35 Yakubovichite is orthorhombic, *Imma*, unit cell parameters of the holotype material: *a* 10.3878(10),

36 *b* 13.0884(10), *c* 6.4794(6) Å, *V* 880.94(2) Å^3, *Z* = 4. Chemical composition of holotype material

37 (electron microprobe, wt.%): Na_2O 1.82, K_2O 1.76, CaO 6.37, SrO 0.49, BaO 1.37, MgO 2.13, NiO

38 21.39, CuO 0.16, Fe_2O_3 18.80, Al_2O_3 1.06, V_2O_3 0.44, Cr_2O_3 0.15, P_2O_5 44.15, total 100.09. The

39 empirical formula calculated on the basis of 12 oxygen atoms per formula unit is:

40 $(Ca_{0.55}Na_{0.29}K_{0.18}Ba_{0.04}Sr_{0.02})_{\Sigma1.08}(Ni_{1.39}Mg_{0.26}Fe^{3+}_{0.24}V^{3+}_{0.03}Cu_{0.01}Cr_{0.01})_{\Sigma1.94}(Fe^{3+}_{0.90}Al_{0.10})_{\Sigma1}P_{3.02}O_{12}$.

41 $D_{calc.}$ = 3.657 g cm^{-3}. The strongest lines of powder XRD pattern [d(Å)(I)(hkl)]: 5.82(44)(011),

42 5.51(73)(101), 5.21(32)(200), 4.214(34)(121), 2.772(97)(240), 2.748(100)(202), 2.599(38)(400).

43 Yakubovichite is the first mineral that crystallizes in the α-$CrPO_4$ structure type. It has a direct

44 synthetic analogue, $CaNi_2Fe^{3+}(PO_4)_3$. Since yakubovichite is the first natural Ni-phosphate of non-

45 meteoritic origin, the possible sources of Ni in the reported mineral assemblages are discussed.

46 Pyrometamorphic rocks of the Hatrurim Formation were formed at the expense of the sediments

47   belonging to a Cretaceous-Paleogene (Cretaceous-Tertiary) boundary (~66 Ma age). This geological

48   frame marks the event of mass extinction of biological species on Earth that was likely caused by

49   the Chicxulub impact event. The anomalous enrichment of pyrometamorphic assemblages in Ni may

50   be related to metamorphic assimilation of Ni-rich minerals accumulated in the Cretaceous-

51   Paleogene layer, which was formed due to a Chicxulub collision.

52

53   **Keywords:** nickel, phosphate, phosphide, trevorite, bunsenite, escolaite, crystal structure,

54   pyrometamorphism, Dead Sea Transform Fault, Hatrurim Formation, Cretaceous-Paleogene

55   boundary

56

Introduction

57

58   Nickel in metallogenic provinces on Earth behaves as a typical chalcophile element, with a strong

59   affinity to sulfide and arsenide ores (Meyer 1968). The world largest Cu-Ni-PGE sulfide deposits

60   that are confined to ultrabasic complexes, such as Norilsk-Talnakh in Russia (Barnes et al. 2020),

61   Sudbury in Canada (Hawley 1962), Cu-Ni ore fields in Australia (Hoatson et al. 2006), as well as

62   Ni-laterites formed by the weathering of sulfide-bearing ultramafites (Thorne et al. 2012) provide

63   ~90% of Ni world production (Meyer 1968). In XIX-XX centuries, Ni deposits belonging to a so-

64   called five-element, or Ag–Bi–Co–Ni–U formation, with predominance of Ni-Co arsenide ores,

65   were very important. The ore fields of this type are widespread in Canada (Petruk 1971). However,

66   the most famous and best studied five-element mining district is an Erzgebirge area, which

67   encompasses numerous, now abandoned shafts in Saxony (Germany) and Jáchymov (St.

68   Joachimsthal) in Czech Republic (Ondruš et al. 2003; Guilcher et al. 2021).

69   The speciation of secondary minerals in the oxidation zones of ore deposits is largely

70   determined by the composition of primary ores. Therefore, it is not surprising that the most diverse

71   group among secondary Ni minerals is arsenates, counting 17 valid species (www.mindat.org,

72   accessed August 2022). One could expect that phosphorus, as a nearest chemical analogue of

73   arsenic, could also couple with Ni in the oxidation zone to form corresponding phosphates.

74   However, there were only two Ni phosphate minerals reported until last decade – cassidyite,

75   $Ca_2Ni(PO_4)_2 \cdot 2H_2O$, and arupite $Ni_3(PO_4)_2 \cdot 8H_2O$. Both minerals have rather exotic origin – they are

76   the products of terrestrial weathering of iron meteorites. Cassidyite was discovered among

77   secondary mineral assemblages of the Wolf Creek meteorite crater in Victoria, Western Australia

78   (White et al. 1967), whereas arupite originates from the oxidation crust of the world biggest Ni-rich

79   ataxite – the Santa Catharina meteorite, Brazil (Buchwald 1975; 1990). Recently, we briefly

80   introduced the readers with a novel type of terrestrial phosphate mineralization – the assemblages

4

81 formed by pyrolytic oxidation of natural phosphides in the Hatrurim Formation, the area confined to

82 the Dead Sea Transform fault system (Britvin et al. 2021a). The specific feature of reported

83 associations is an anomalous enrichment in Ni. In the present paper, we provide the first

84 mineralogical description of a new Ni phosphate from these localities. The mineral is named

85 yakubovichite (cyrillic spelling - якубовичит), in honor of Prof. Olga Vsevolodovna Yakubovich

86 (born 1950), a prominent Russian crystal chemist, for her contributions to the studies of inorganic

87 phosphates. Olga Yakubovich is an author of more than 100 articles devoted to the crystal chemistry

88 of phosphates (e.g., Yakubovich et al. 2021 and other articles). The mineral and its name have been

89 approved by the Commission on New Minerals, Nomenclature and Classification (CNMNC) of the

90 International Mineralogical Association (IMA 2020-094). The holotype specimen of yakubovichite

91 is deposited in the collections of the Fersman Mineralogical Museum of the Russian Academy of

92 Sciences, Moscow, Russia, with the registration number 5626/1.

93

94 **Analytical methods**

95 ***Electron microprobe analysis***

96 Chemical composition of yakubovichite and associated minerals was determined on polished and

97 carbon-coated thin sections using an INCA WAVE 500 WDX spectrometer (20 kV, 10 nA) attached

98 to a Hitachi S-3400N SEM. The following standards were used ($K\alpha$ lines): chkalovite (Na), diopside

99 (Ca, Si), microcline (K), celestine (Sr), cuprite (Cu), chromite (Cr), V_2O_3 (V), hematite (Fe),

100 trevorite (Ni), gehlenite (Al), rutile (Ti), Co metal (Co), and chlorapatite (P). Ba$L\alpha$ was measured

101 with barite.

102 ***Single-crystal X-ray diffraction (SCXRD) and powder diffraction (PXRD)***

103 SCXRD data collection was performed with a Bruker Kappa APEX DUO CCD diffractometer

104 (microfocus tube, Mo$K\alpha$ radiation). Subsequent data processing and integration procedures were

105   carried out using Rigaku Oxford Diffraction CrysAlisPro software (Rigaku Oxford Diffraction). The

106   crystal structure was solved and refined to $R_1 = 0.029$ using *SHELX*-2018 program package

107   (Sheldrick 2015) incorporated into Olex2 graphic user shell (Dolomanov et al. 2009). The complete

108   set of data collection and structure refinement details can be retrieved from crystallographic

109   information file (CIF) in Supplementary Data. PXRD patterns of yakubovichite and bunsenite were

110   acquired using a Rigaku RAXIS Rapid II diffractometer. The instrument uses rotating anode (Co$K\alpha$,

111   40 kV, 15 mA), microfocus mirror monochromator and semi-cylindrical imaging plate detector ($r =$

112   127.4 mm), and is set up in the Debye-Scherrer geometry. A plate-to-profile data conversion was

113   carried out with osc2xrd program (Britvin et al. 2017). The unit-cell parameters refinement and

114   theoretical pattern calculation was performed with Stoe WinXPOW software (Stoe and Cie GmbH).

115   ***Raman spectroscopy***

116   The Raman spectrum of yakubovichite was obtained by means of a LabRam HR 800 (Horiba Jobin–

117   Yvon) Raman spectrometer with He-Ne laser excitation (632.8 nm). The ~1mW laser beam was

118   focused by 100× objective at the Olympus BX41 confocal microscope, to a point of approximately 2

119   μm^2. The aperture diameter was set to 150 μm, and the 600 gr/mm grating was used. Accumulation

120   time was 150 seconds with 4 repetitive scans.

121

Nickel mineralization in the Hatrurim Formation

123   Yakubovichite was discovered in the Hatrurim Formation – the world's largest

124   pyrometamorphic complex whose outcrops are exposed in the area of 150×200 km^2 across the Dead

125   Sea Transform fault system (e.g., Ben-Avraham et al. 2008), in Israel, Palestinian Authority and

126   Jordan. Geological setting, stratigraphy and the origin of this complex, also known as the Mottled

127   Zone, was reviewed in previous works (Gross 1977; Burg et al. 1992; Vapnik et al. 2007; Novikov

128   et al. 2013; Abzalov et al. 2015). Pyrometamorphic lithologies were formed through the extensive

6

129   high-temperature calcination and fusion of chalky-marly sedimentary sequences of late Cretaceous -

130   early Paleogene age (e.g., Britvin et al. 2022b). Elevated Ni contents (up to hundreds ppm) were

131   reported in these sediments both in Israel and Jordan (e.g., Issar et al. 1969; Ilani et al. 1985; Gilat

132   1994; Bogoch et al. 1999; Fleurance et al. 2013), but the mineralogical speciation of Ni was not

133   investigated. The unique Ni-bearing phosphide mineralization, discovered in the Mottled Zone for

134   the last decade, obviously originates from metamorphosed Ni-enriched sedimentary beds (Britvin et

135   al. 2015, 2020c, 2022a). Besides phosphides, Ni in this rock complex tends to concentrate in oxide

136   minerals.

137   *Trevorite*, $NiFe_2O_4$, a rare spinel-group mineral, was initially discovered in anomalous Ni

138   oxide ore of the Bon Accord orebody, Kaapvaal craton, Barberton greenstone belt, South Africa

139   (Walker 1923; De Waal 1972). Subsequently, it was reported in peridotites of the Mount Clifford

140   deposit, Western Australia (Hudson and Travis 1981), pyroxenites of the Baikal rift zone, Russia

141   (Muravyeva and Senin 1993), in the Mid-Ocean ridge basalt, Pacific Ocean (Pandey et al. 2008) and

142   in impact melt veins of the Morokweng impact structure, South Africa (e.g., Koerbl et al. 1997). In

143   the Hatrurim Formation, trevorite was briefly mentioned with no supplemental analytical data

144   (Sharygin et al. 2013; Krzątała et al. 2020). We detected trevorite in phosphide-bearing assemblages

145   of the Hatrurim Formation on both Israel and Jordan sides of the Dead Sea basin. In the Halamish

146   wadi, Hatrurim basin, Israel, trevorite was found as an accessory mineral in diopside paralava,

147   where it forms euhedral crystals up to 30 μm associated with keplerite $Ca_9Mg(Ca_{0.5}\square_{0.5})(PO_4)_7$

148   (Britvin et al. 2021b), hematite, and diopside (Fig. 1). In the type locality of yakubovichite – an

149   abandoned phosphorite quarry in the Daba-Siwaqa complex, Transjordan Plateau, Jordan (31° 21'

150   52" N, 36° 10' 55" E), trevorite was found in clinopyroxene-plagioclase paralava containing

151   phosphides - nickolayite, FeMoP (Murashko et al. 2022), and orishchinite, $(Ni,Fe,Mo)_2P$ (Britvin et

152   al. 2022c). Representative chemical compositions of trevorite are provided in Table 1. The mineral

7

153 has varying chemical composition, but the intragrain zoning has never been observed. An interesting

154 feature of trevorite from the Hatrurim Formation is that it is completely devoid of Mg. It is

155 noteworthy that, with NiO contents of 30 wt.%, this trevorite is the most Ni-rich variety of the

156 mineral in nature (cf. Beckett-Brown and McDonald 2018).

157 *Bunsenite*, a naturally occurring NiO, was discovered at Johanngeorgenstadt, Erzgebirge,

158 Saxony, Germany, within the specific mineral assemblages formed by the "dry oxidation" of Ni

159 arsenide ores of the Ag–Bi–Co–Ni–U formation (Bergemann 1858; Roberts et al. 2001, 2004).

160 Subsequently, the mineral was described in association with trevorite in the above-mentioned Bon-

161 Accord orebody (De Waal 1972). Other reported occurrences (www.mindat.org, accessed August

162 2022) require additional confirmation. Bunsenite, like trevorite, was previously mentioned in the

163 Hatrurim Formation (Khoury 2020), but without analytical data. We have found bunsenite in the

164 phosphorite quarry in the Daba-Siwaqa complex, Jordan, where it occurs in phosphide-bearing

165 clinopyroxene-plagioclase paralava. The mineral forms unusual amoeboid-shaped incrustations,

166 surrounding microcavities within trevorite veinlets and rims, which are embedded into Ni-bearing

167 hematite (Fig. 2). Bunsenite grains extracted from the paralava have a deep apple-green colour.

168 Chemical composition of the mineral, along with composition of associated trevorite and hematite,

169 is given in Table 1. Structural identity of bunsenite was confirmed with powder X-ray diffraction

170 pattern, which contains the following lines [d(Å)(I)(hkl)]: 2.4135(75)(111), 2.0896(100)(200),

171 1.4774(30)(220), 1.2599(10)(311), 1.2064(6)(222), 1.0447(2)(400), 0.9588(2)(331). The refined a

172 parameter value is 4.1793(2) Å, $V = 72.995(4)$ Å^3.

173 *Hematite–Eskolaite series* $Fe_2O_3 – Cr_2O_3$. Nickeliferous members of the solid solution

174 hematite-eskolaite are common in phosphide-phosphate-bearing assemblages, both in Israel and

175 Jordan. They form granular aggregates composed of euhedral to platy crystals, disseminated within

176 clinopyroxene-plagioclase paralavas (Fig. 1 and 2). Representative chemical compositions are

8

177   presented in Table 1. The minerals contain up to 2 wt.% NiO. Their structural identity (hematite

178   structural type) was confirmed by means of electron backscatter diffraction of representative grains.

179   Intermediate oxides of hematite-eskolaite series are known in nature and as synthetic

180   compounds (e.g., Pérez-Cruz et al. 2015). The possibility of Ni incorporation into hematite was

181   demonstrated on synthetic samples with up 2 wt.% Ni (Frierdich et al. 2011; Gadol et al. 2017).

182   However, to the best of our knowledge, Ni contents in natural hematite are everywhere below

183   detection limit of electron microprobe analysis. Therefore, nickeliferous hematite-eskolaite minerals

184   from the Hatrurim Formation are likely the most Ni-rich varieties encountered in nature.

185   It is noteworthy that Ni-bearing oxides described above, Ni-phosphides and phosphates,

186   including yakubovichite, are confined to the same type of rocks – diopside-clinopyroxene paralavas

187   developed at the extent of the sedimentary beds of Cretaceous-Paleogene age. The possible sources

188   of Ni in these rocks are discussed in this article.

189

190   **Occurrence, appearance and physical properties of yakubovichite**

191   Yakubovichite was discovered in paralavas (fused sedimentary rocks) exposed in the

192   abandoned phosphorite quarry in the Daba-Siwaqa pyrometamorphic complex, Jizah District,

193   Amman Governorate, Jordan (31° 21' 52" N, 36° 10' 55" E). The host paralava consists almost

194   entirely of aggregates of long-prismatic colorless diopside crystals up to 1×5 mm in size, with rare

195   anorthite, secondary calcite and hydrous Ca-silicates infilling the interstices between diopside

196   crystals. Diopside has nearly ideal $CaMgSi_2O_6$ composition, with Fe and Al contents below 0.05

197   wt.%. The most common accessory mineral is microcrystalline hematite. Phosphate-phosphide

198   assemblages form irregularly shaped centimeter-sized nests in paralava, and consist of hematite,

199   crocobelonite $CaFe_2^{3+}(PO_4)_2O$ (IMA 2020-005), Ni-phosphides – negevite NiP_2, halamishite Ni_5P_4,

200   and transjordanite Ni_2P (Britvin et al. 2020a,b,c), and Fe-Ni bearing phosphates (Fig. 3).

9

201 Yakubovichite forms polycrystalline segregations up to 0.2 mm in size composed of equant crystal

202 grains, in association with crocobelonite, hematite, other phosphates and phosphides (Fig. 3). The

203 mineral has a deep yellow to lemon-yellow colour (typical of anhydrous Ni-bearing phosphates) and

204 yellowish-white strike. It is transparent to translucent with vitreous luster. Yakubovichite has no

205 cleavage; Mohs hardness = 4. Density, calculated based on the empirical formula and unit-cell

206 parameters refined from X-ray single-crystal data, is 3.657 g cm^{-3}. In thin sections and in immersion

207 liquids in transmitted light, yakubovichite has pale-yellow to lemon-yellow colour, depending on

208 grain thickness. It is non-pleochroic. In crossed polars, yakubovichite grains exhibit undulatory

209 extinction that prevents from estimations of 2V value. Biaxial (−), $2V_{calc}$ = 38°, α = 1.725(3), β =

210 1.765(3), γ = 1.775(3). The Gladstone-Dale compatibility index (Mandarino 1976), 1-(K_P/K_C) =

211 0.011 (superior).

212 Since the approval of yakubovichite by CNMNC, IMA, yakubovichite was also recognized

213 in phosphide-phosphate assemblages found in the Halamish Wadi, Hatrurim Basin, Negev desert,

214 Israel (detailed description of locality is given in: Britvin et al. 2015, 2022b). The association of

215 yakubovichite from the Halamish Wadi is very similar to that of the holotype material from Jordan,

216 but the mineral grains are rather small (less than 10 μm). The structural identity of the mineral from

217 the Halamish Wadi was confirmed using electron backscatter diffraction method.

218

219 **Chemical composition**

220 Electron microprobe data for yakubovichite are summarized in Table 2. It can be seen that

221 chemical composition of the mineral from Jordan (the holotype) is very similar to that of

222 yakubovichite from Israel. All iron was assumed to be Fe^{3+}, according to the results of bond-valence

223 calculations for holotype yakubovichite (bond-valence sum for Fe site is 3.07 valence units, Table

224 3). Element grouping in the empirical formula of the mineral was performed according to the

225   stoichiometry of $CaNi_2Fe^{3+}(PO_4)_3$ – the synthetic analogue of yakubovichite (Ouaatta et al. 2017).

226   The empirical formula of holotype yakubovichite based on 12 oxygen atoms per formula unit is

227      $(Ca_{0.55}Na_{0.29}K_{0.18}Ba_{0.04}Sr_{0.02})_{1.08}(Ni_{1.39}Mg_{0.26}Fe^{3+}_{0.24}V^{3+}_{0.03}Cu_{0.01}Cr_{0.01})_{1.94}(Fe^{3+}_{0.90}Al_{0.10})_{1.00}P_{3.02}O_{12}$.

228   The formula of the mineral from Israel is:

229      $(Ca_{0.63}Na_{0.23}K_{0.11}Ba_{0.08}Sr_{0.02})_{1.07}(Ni_{1.30}Mg_{0.41}Fe^{3+}_{0.16}V^{3+}_{0.06}Cu_{0.01}Cr_{0.01})_{1.95}(Fe^{3+}_{0.94}Al_{0.06})_{1.00}(P_{3.00}Si_{0.02}$

230      $)_{3.02}O_{12}$. The ideal formula of yakubovichite is $CaNi_2Fe^{3+}(PO_4)_3$.

231

Crystal structure and powder X-ray diffraction

233   Yakubovichite is the first mineral that crystallizes in the α-$CrPO_4$ structure type (Attfield et

234   al. 1988). The crystal structure was solved and refined on the holotype material from the Jordan

235   locality. It represents a framework built up of corner- end edge-sharing [MO_6] octahedra, and [PO_4]

236   tetrahedra (Fig. 4). The two kinds of channels penetrate the structure along the a- and b-axes,

237   respectively. The channels are filled with alkali-earth and alkali cations (the eight-fold coordinated A

238   ($4e$) site), whereas in α-$CrPO_4$ the corresponding channels are vacant. The octahedrally coordinated

239      $M1$ ($4a$) site is predominantly populated by Fe^{3+}, whereas the $M2$ ($8g$) site is Ni-dominant (Table 3).

240   The bond-valence sums for corresponding metal and phosphorus sites are well consistent with

241   formal cation charges calculated based on the empirical formula (Table 3). There is a direct

242   synthetic analogue of yakubovichite, $CaNi_2Fe^{3+}(PO_4)_3$ (Ouaatta et al. 2017), and its Sr counterpart,

243      $SrNi_2Fe^{3+}(PO_4)_3$ (Ouaatta et al. 2015) (Table 4). The powder X-ray diffraction pattern of

244   yakubovichite is given in Table 5.

245

Raman spectroscopy

247   The Raman spectrum of yakubovichite is consistent with its chemical composition and

248   structure, as an anhydrous orthophosphate (Nakamoto 2008). The fingerprint region (Fig. 5a)

249   contains the following bands (cm^{-1}): 105, 142, 173, 187, 198, 228, 259, 290, 324, 378 ([MO_6] and

250   lattice modes); 416, 471, 495 [v_2 (symmetric bending (PO_4) vibrations]; 542, 560, 590, 629, 664,

251   742 [v_4 (asymmetric bending (PO_4) modes]; 936 [v_1 (symmetric stretching P-O)]; 1040, 1054, 1100,

252   1141 [v_3 (asymmetric stretching P-O)]. From the chemical point of view, the absence of bands in the

253   O–H stretching region (3800–3000 cm^{-1}) and bending modes corresponding to molecular H_2O

254   (1630–1670 cm^{-1}) (Fig. 5b) evidences that the mineral does not contain water, that corroborates with

255   electron microprobe analyses, crystal structure and optical data.

256

257   **Discussion: structural links between yakubovichite, galileiite and xenophyllite**

258   The possible structural analogues of yakubovichite are the two meteoritic minerals, galileiite

259   (Olsen and Steele 1997) and xenophyllite (Britvin et al. 2020d). Unfortunately, the crystal structures

260   of both species were not determined; therefore, one can only rely on the chemical composition, X-

261   ray powder diffraction data and unit-cell parameters (Table 4). Galileiite was described as a new

262   mineral from several IIIAB group iron meteorites with a proposed formula $NaFe_4^{2+}(PO_4)_3$ (Olsen

263   and Steele 1997; Olsen et al. 1999), and was reported from other iron and chondritic meteorites

264   (Chen and Xie 1996; Sugiura and Hoshino 2003; Xie et al. 2014; Sharygin et al. 2016). Based on the

265   X-ray powder diffraction pattern, the mineral was ascribed to the fillowite group (Olsen and Steele

266   (1997). However, the authors have noted that the pattern indexing in the fillowite unit cell was not

267   entirely satisfactory, and the assertion of galileiite as a mineral belonging to the fillowite group "is

268   yet to be demonstrated" (Olsen and Steele 1997). It should be noted that such a demonstration was

269   not yet completed; therefore, the assignment of galileiite to either structural type (or mineral group)

270   is a debatable question, since the synthetic chemical analogue of galileiite, $Na_{1.1}Fe_4(PO_4)_3$ (Zhang et

271   al. 2018) adopts a distorted α-CrPO$_4$ structure (Table 4).

272   Xenophyllite, ideally $Na_4Fe_7(PO_4)_6$, is another meteoritic phosphate discovered in the IIIAB

273   iron meteorite, Augustinovka (Britvin et al. 2020d). The chemical formula of the mineral, its space

274   group and unit-cell parameters are consistent with those of synthetic phosphates $ANa_3M_7(PO_4)_6$

275   where A = K, Rb, Cs; M = Fe^{2+}, Mg, Mn, Zn (Yakubovich et al. 1996; Queen et al. 2007; Guo et al.

276   2014; Ben Hamed et al. 2017). The direct chemical analogue of xenophyllite was reported by Pu et

277   al. (2019). All these compounds represent variations of the α-$CrPO_4$ structure type (Britvin et al.

278   2020d). Moreover, there is a continuous series of solid solutions between xenophyllite,

279    $Na_4Fe_7(PO_4)_6$, and the α-$CrPO_4$-related mineral with the chemical formula of $Na_2Fe_8(PO_4)_6$ – i.e.,

280   the formula of galileiite. The possible structural relationships between xenophyllite, galileiite and α-

281    $CrPO_4$ were discussed by Britvin et al. (2020d).

282

283   **Formation conditions of yakubovichite**

284   Pyrometamorphic processes that dominated during the formation of yakubovichite-bearing

285   assemblages, imply the high-temperature oxidative environment, near-atmospheric pressure, and the

286   lack of water in the system. The synthetic analogue of yakubovichite, $CaNi_2Fe^{3+}(PO_4)_3$, was prepared

287   by crystallization from dry phosphate melt fused at 1160 °C (Ouatta et al. 2017). This temperature

288   looks reasonable for the conditions that expectedly occurred during the setup of the Hatrurim

289   Formation (Gross 1977; Burg et al. 1992; Vapnik et al. 2007). The association with Ni-phosphides –

290   negevite NiP_2, halamishite Ni_5P_4 and transjordanite Ni_2P – evidences that yakubovichite might be

291   formed as a result of pyrolytic oxidation (dry roasting) of these phosphides. The latter process could

292   be accompanied by side reactions with Ca-bearing minerals – calcite, lime or fluorapatite, – which

293   served as a source of Ca. In this respect, formation conditions of yakubovichite might resemble

294   those that likely occurred during the formation of anhydrous Ni-arsenates in the oxidized ores of the

295   Erzgebirge mining district (Roberts et al. 2001, 2004; Kampf et al. 2020). The similar (but less hot)

13

296   conditions occur within oxidizing-type arsenate fumaroles of the Tolbachik volcano, Kamchatka

297   Peninsula, Russia (Pekov et al. 2018).

298

299   **Geological implications**

300   As it was pointed out in the introduction, Ni on Earth is an element characteristic of

301   ultramafic complexes and in particular, sulfide ores associated with these formations. In addition, Ni

302   is a mandatory constituent of Fe-Ni metal in iron and stony-iron meteorites, which are accepted to

303   represent the inner parts of small planetary bodies (planetesimals) (Buchwald 1975). These

304   geochemical and cosmochemical reservoirs of Ni can sometimes be interconnected. As an example,

305   there is a consensus that the Sudbury structure in Canada, which hosts the world largest Fe-Ni

306   sulfide deposits, is of meteoroid impact origin (Grieve and Therriault 2000). The anomalous Bon-

307   Accord orebody, known for the extreme Ni enrichment, is considered by several researchers as a

308   metamorphically assimilated iron meteorite (O'Driscoll et al. 2014). Yakubovichite, with 20 wt.%

309   NiO in the chemical composition, comprises the extremely Ni-rich phosphate assemblages whose

310   origin has no obvious links to the above mentioned Ni sources. The same is valid for other Ni-rich

311   minerals in the Hatrurim Formation – Ni-phosphides, bunsenite NiO, trevorite $FeNi_2O_4$ or

312   nickeliferous members of the hematite-eskolaite series, Fe_2O_3-Cr_2O_3. There are no ultrabasic

313   complexes in the territory of Southern Levant. Mineralogical records of a possible high-pressure

314   (impact) event, which could trigger pyrometamorphic processes in the Dead Sea Transform fault

315   system, were reported (Britvin et al. 2021c, 2022d), but there are no geological evidences that could

316   support mineralogical data.

317   The elevated Ni contents in the Cretaceous-Paleogene sediments – the protoliths of

318   pyrometamorphic lithologies – were ascribed to hydrothermal activity related to the development of

319   the Dead Sea Transform fault system (Fleurance et al. 2013). In this respect, we would like to focus

14

320   on the fact that pyrometamorphic rocks of the Hatrurim Formation were developed at the expense of

321   the sediments belonging to a Cretaceous-Paleogene (Cretaceous-Tertiary) boundary (Fig. 6). On the

322   geological timescale, this boundary, ~66 Ma age, marks the period of mass extinction of living

323   species, and is commonly associated with the catastrophic Earth-meteorite collision occurred at the

324   Chicxulub impact crater (Alvarez et al. 1980; Smit 1999; Grieve and Therriault 2000). The elevated

325   Ni contents in the Cretaceous-Paleogene boundary layer are connected with the presence of impact

326   spherules, which contain abundant Ni-bearing spinels enriched in trevorite component (Kyte and

327   Smit 1986; Robin et al. 1992). The corresponding mineralogical studies of the Cretaceous-

328   Paleogene boundary layer in the Southern Levant might shed light on the origin of anomalous Ni

329   mineralogy in pyrometamorphic lithologies of the Hatrurim Formation.

330

340

341   **References**

342   Abzalov, M.Z., Heyden, A., van der, Saymeh, A., and Abuqudaira, M. (2015) Geology and

343   metallogeny of Jordanian uranium deposits. Applied Earth Science, 124, 63–77.

15

344   Alvarez, L.W., Alvarez, W., Asaro, F., and Michel, H.V. (1980) Extraterrestrial cause for the

345   Cretaceous-Tertiary extinction. Science, 208, 1095–1108.

346   Attfield, J.P., Cheetham, A.K., Cox, D.E., and Sleight, A.W. (1988) Synchrotron X-ray and neutron

347   powder diffraction studies of the structure of α-CrPO$_4$. Journal of Applied Crystallography, 21,

348   452–457.

349   Barnes, S.J., Malitch, K.N., and Yudovskaya, M.A. (2020) Introduction to the special issue on the

350   Norilsk-Talnakh Ni-Cu-platinum group element deposits. Economic Geology, 115, 1157–

351   1172.

352   Begg, G.C., Hronsky, J.M.A., Arndt, N.T., Griffin, W.L., OReilly, S.Y., and Hayward, N. (2010)

353   Lithospheric, cratonic and geodynamic setting of Ni-Cu-PGE sulfide deposits. Economic

354   Geology 105, 1057–1070.

355   Beckett-Brown, C.E., and McDonald, A.M. (2018) The crystal-chemistry of Ni-bearing spinel-group

356   minerals: Chemical, geological and exploration implications. Canadian Mineralogist 56, 77–

357   94.

358   Ben-Avraham, Z., Garfunkel, Z., and Lazar, M. (2008) Geology and evolution of the Southern Dead

359   Sea Fault with emphasis on subsurface structure. Annual Review of Earth and Planetary

360   Sciences, 36, 357–387.

361   Ben Hamed, T., Boukhris, A., Badri, A., and Ben Amara, M. (2017) Synthesis and crystal structure

362   of a new magnesium phosphate Na$_3$RbMg$_7$(PO$_4$)$_6$. Acta Crystallographica, E73, 817−812.

363   Bergemann, C. (1858) Ueber einige Nickelerze. Journal für Praktische Chemie, 75, 239–244.

364   Bogoch, R., Gilat, A., Yoffe, O., and Ehrlich, S. (1999). Rare earth trace element distributions in the

365   Mottled Zone complex, Israel. Israel Journal of Earth Sciences, 48, 225–234.

366   Brese, N.E., and O'Keeffe, M. (1991) Bond-valence parameters for solids. Acta Crystallographica,

367   B47, 192–197.

368   Britvin, S.N., Murashko, M.N., Vapnik, Ye., Polekhovsky, Yu.S., and Krivovichev, S.V. (2015)

369   Earth's phosphides in Levant and insights into the source of Archaean prebiotc phosphorus.

370   Scientific Reports, 5, 8355.

371   Britvin, S.N., Dolivo-Dobrovolsky, D.V., and Krzhizhanovskaya, M.G. (2017) Software for

372   processing the X-ray powder diffraction data obtained from the curved image plate detector of

373   Rigaku RAXIS Rapid II diffractometer. Zapiski Rossiiskogo Mineralogicheskogo

374   Obshchestva, 146(3), 104–107 (in Russian).

375   Britvin, S.N., Murashko, M.N., Vapnik, Ye., Polekhovsky, Yu.S., Krivovichev, S.V.,

376   Krzhizhanovskaya, M.G., Vereshchagin, O.S., Shilovskikh, V.V., and Vlasenko, N.S. (2020a)

377   Transjordanite, Ni_2P, a new terrestrial and meteoritic phosphide, and natural solid solutions

378   barringerite–transjordanite (hexagonal Fe_2P–Ni_2P). American Mineralogist, 105, 428–436.

379   Britvin, S.N., Murashko, M.N., Vapnik, Ye., Polekhovsky, Yu.S., Krivovichev, S.V., Vereshchagin,

380   O.S., Shilovskikh, V.V., Vlasenko, N.S., and Krzhizhanovskaya, M.G. (2020b) Halamishite,

381   Ni_5P_4, a new terrestrial phosphide in the Ni–P system. Physics and Chemistry of Minerals,

382   2020, 3.

383   Britvin, S.N., Murashko, M.N., Vapnik, Ye., Polekhovsky, Yu.S., Krivovichev, S.V., Vereshchagin,

384   O.S., Shilovskikh, V.V., and Krzhizhanovskaya, M.G. (2020c) Negevite, the pyrite-type NiP_2,

385   a new terrestrial phosphide. American Mineralogist, 105, 422–427.

386   Britvin, S.N., Krivovichev, S.V., Obolonskaya, E.V., Vlasenko, N.S., Bocharov, V.N., and

387   Bryukhanova, V.V. (2020d) Xenophyllite, $Na_4Fe_7(PO_4)_6$, an exotic meteoritic phosphate: new

388   mineral description, Na-ions mobility and electrochemical implications. Minerals, 10, 300.

389   Britvin, S.N., Murashko, M.N., Vapnik, Ye., Vlasenko, N.S., Krzhizhanovskaya, M.G.,

390   Vereshchagin, O.S., Bocharov, V.N., and Lozhkin, M.S. (2021a) Cyclophosphates, a new class

17

391   of native phosphorus compounds, and some insights into prebiotic phosphorylation on early

392   Earth. Geology, 49, 382–386.

393   Britvin, S.N., Galuskina, I.O., Vlasenko, N.S., Vereshchagin, O.S., Bocharov, V.N.,

394   Krzhizhanovskaya, M.G., Shilovskikh, V.V., Galuskin, E.V., Vapnik, Ye., and Obolonskaya,

395   E.V. (2021b) Keplerite, $Ca_9(Ca_{0.5}\square_{0.5})Mg(PO_4)_7$, a new meteoritic and terrestrial phosphate

396   isomorphous with merrillite, $Ca_9NaMg(PO_4)_7$. American Mineralogist, 106, 1917–1927.

397   Britvin, S.N., Vereshchagin, O.S., Shilovskikh, V.V., Krzhizhanovskaya, M.G., Gorelova, L.A.,

398   Vlasenko, N.S., Pakhomova, A.S., Zaitsev, A.N., Zolotarev, A.A., Bykov, M., Lozhkin, M.S.,

399   and Nestola, F. (2021c) Discovery of terrestrial allabogdanite $(Fe,Ni)_2P$, and the effect of Ni

400   and Mo substitution on the barringerite-allabogdanite high-pressure transition. American

401   Mineralogist, 106, 944–952.

402   Britvin, S.N., Murashko, M.N., Krzhizhanovskaya, M.G., Vereshchagin, O.S., Vapnik, Ye.,

403   Shilovskikh, V.V., Lozhkin, M.S., and Obolonskaya, E.V. (2022a) Nazarovite, $Ni_{12}P_5$, a new

404   terrestrial and meteoritic mineral structurally related to nickelphosphide, Ni_3P. American

405   Mineralogist, doi:10.2138/am-2022-8219.

406   Britvin, S.N., Murashko, M.N., Vereshchagin, O.S., Vapnik, Ye., Shilovskikh, V.V., Vlasenko,

407   N.S., and Permyakov, V.V. (2022b) Expanding the speciation of terrestrial molybdenum:

408   discovery of polekhovskyite, $MoNiP_2$, and insights into the sources of Mo-phosphides in the

409   Dead Sea Transform area, American Mineralogist, doi:10.2138/am-2022-8261.

410   Britvin, S.N., Murashko, M.N., Vapnik, Y., Zaitsev, A.N., Shilovskikh, V.V., Vasiliev, E.A.,

411   Krzhizhanovskaya, M.G., and Vlasenko, N.S. (2022c) Orishchinite, a new terrestrial

412   phosphide, the Ni-dominant analogue of allabogdanite. Mineralogy and Petrology,

413   doi:10.1007/s00710-022-00787-x

414 Britvin, S.N., Vlasenko, N.S., Aslandukov, A., Aslandukova, A., Dubrovinsky, L., Gorelova, L.A.,

415   Krzhizhanovskaya, M.G., Vereshchagin, O.S., Bocharov, V.N., Shelukhina, Yu.S., Lozhkin,

416   M.S., Zaitsev, A.N., and Nestola, F. (2022d) Natural cubic perovskite, $Ca(Ti,Si,Cr)O_{3-\delta}$, a

417   versatile potential host for rock-forming and less common elements up to Earth's mantle

418   pressure. American Mineralogist, doi: 10.2138/am-2022-8186

419 Buchwald, V.F. (1975) Handbook of iron meteorites, 3 vols. University of California Press,

420   Berkeley.

421 Buchwald, V.F. (1990) A new mineral, arupite, $Ni_3(PO_4)_2 \cdot 8H_2O$, the nickel analogue of vivianite.

422   Neues Jahrbuch für Mineralogie, Monatshefte, 1990, 76–80.

423 Burg, A., Starinsky, A., Bartov, Y., and Kolodny, Y. (1992) Geology of the Hatrurim Formation

424   ("Mottled Zone") in the Hatrurim basin. Israel Journal of Earth Sciences, 40, 107–124.

425 Chen, M., and Xie, X. (1996) Na behavior in shock-induced melt phase of the Yanzhuang (H6)

426   chondrite. European Journal of Mineralogy, 8, 325–333.

427 De Waal, S.A. (1972) Nickel minerals from Barberton, South Africa: V. Trevorite, redescribed.

428   American Mineralogist, 57, 1524–1527.

429 Dolomanov, O.V., Bourhis, L.J., Gildea, R.J., Howard, J.A., and Puschmann, H. (2009) OLEX2: a

430   complete structure solution, refinement and analysis program, Journal of Applied

431   Crystallography, 42, 339–341.

432 Fleurance, S., Cuney, M., Malartre, M., and Reyx, J. (2013) Origin of the extreme polymetallic

433   enrichment (Cd, Cr, Mo, Ni, U, V, Zn) of the Late Cretaceous–Early Tertiary Belqa Group,

434   central Jordan. Palaeogeography, Palaeoclimatology, Palaeoecology, 369, 201–219.

435 Frierdich, A. J., Luo, Y., and Catalano, J. G. (2011) Trace element cycling through iron oxide

436   minerals during redox-driven dynamic recrystallization. Geology, 39, 1083−1086.

437 Gadol, H. J., Flynn, E. D., and Catalano, J. G. (2017) Oxalate-promoted trace metal release from

438   crystalline iron oxides under aerobic conditions. Environmental Science & Technology

439   Letters, 4, 311−315.

440 Gilat, A. (1994) Tectonic and associated mineralization activity, Southern Judea, Israel. Geological

441   Survey of Israel, Report GSI/19/94, Jerusalem, 322 p.

442 Grieve, R., and Therriault, A. (2000) Vredefort, Sudbury, Chicxulub: Three of a Kind? Annual

443   Reviews in Earth and Planetary Science, 28, 305–338.

444 Gross, S. (1977) The mineralogy of the Hatrurim Formation, Israel. Geological Survey of Israel

445   Bulletin, 70, 1–80.

446 Guilcher, M., Schmaucks, A., Krause, J., Markl, G., Gutzmer, J., and Burisch, M. (2021) Vertical

447   zoning in hydrothermal U-Bi-Co-Ni-As-Ag systems - a case study from the Annaberg-

448   Buchholz district, Erzgebirge (Germany). Economic Geology, 116, 1893–1915.

449 Guo, W., He, Z., Zhang, S., Yang, M., Tang, Y., and Cheng, W. (2014) $KNa_3Mn_7(PO_4)_6$: 2D spin-

450   frustrated magnetic material with a diamond-like chain structure. RSC Advances, 4,

451   21559−21562.

452 Hawley, J.E. (1962) The Sudbury ores: their mineralogy and origin. Canadian Mineralogist, 7, 1–

453   202.

454 Hoatson, D.M., Jaireth, S., and Jaques, A.L. (2006) Nickel sulfide deposits in Australia:

455   Characteristics, resources, and potential. Ore Geology Reviews, 29, 177–241.

456 Hudson, D.R., and Travis, G.A. (1981) A native nickel-heazlewoodite-ferroan trevorite assemblage

457   from Mount Clifford, western Australia. Economic Geology, 76, 1686–1697.

458 Ilani, S., Kronfeld, J., and Flexer, A. (1985) Iron-rich veins related to structural lineaments, and the

459   search for base metals in Israel. Journal of Geochemical Exploration, 24, 197–206.

460   Issar, A., Eckstein, Y., and Bogoch, R. (1969) A possible thermal spring deposit in the Arad area,

461   Israel. Israel Journal of Earth Sciences, 18, 17–20.

462   Kampf, A.R., Nash, B.P., Plášil, J., Smith, J.B., and Feinglos, M.N. (2020) Niasite and

463   johanngeorgenstadtite, $Ni^{2+}_{4.5}(AsO_4)_3$ dimorphs from Johanngeorgenstadt, Germany. European

464   Journal of Mineralogy, 32, 373–385.

465   Khoury, H.N. (2020) High- and low-temperature mineral phases from the pyrometamorphic rocks,

466   Jordan. Arabian Journal of Geosciences, 13, 734.

467   Kyte, F.T., and Smit, J. (1986) Regional variations in spinel compositions: An important key to the

468   Cretaceous/Tertiary event. Geology, 14, 485–487.

469   Koeberl, C., Armstrong, R.A., and Reimold, W.U. (1997) Morokweng, South Africa: A large impact

470   structure of Jurassic-Cretaceous boundary age. Geology, 25, 731–734.

471   Krząteła, A., Krüger, B., Galuskina, I., Vapnik, Y., and Galuskin, E. (2020) Walstromite,

472        $BaCa_2(Si_3O_9)$, from rankinite paralava within gehlenite hornfels of the Hatrurim Basin, Negev

473   Desert, Israel. Minerals, 10, 407.

474   Muravyeva, N.S., and Senin, V.G. (1993) Trevorite in pyroxenite nodules from the Tokinsky

475   Stanovik Mountains (ENE prolongation of Baikal rift zone). Mineralogical Magazine, 57,

476   171–173.

477   Mandarino, J.A. (1976) The Gladstone-Dale relationship. Part I: Derivation of new constants.

478   Canadian Mineralogist, 14, 498–502.

479   Meyer, C. (1968) Ore Deposits. Nickel. International Geological Review – Book Series, 10, 72–82.

480   Murashko, M.N., Britvin, S.N., Vapnik, Y., Polekhovsky, Y.S., Shilovskikh, V.V., Zaitsev, A.N.,

481   Vereshchagin, O.S. (2022) Nickolayite, FeMoP, a new natural molybdenum phosphide.

482   Mineralogical Magazine, doi doi:10.1180/mgm.2022.52

483 Nakamoto K. (2008) Infrared and Raman Spectra of Inorganic and Coordination Compounds,

484 Theory and Applications in Inorganic Chemistry. John Wiley and Sons, New York.

485 Novikov, I., Vapnik, Ye., and Safonova, I. (2013) Mud volcano origin of the Mottled Zone,

486 Southern Levant. Geoscience Frontiers, 4, 597–619.

487 O'Driscoll, B., Clay, P.L., Cawthorn, R.G., Lenaz, D., Adetunji, J., and Kronz, A. (2014) Trevorite:

488 Ni-rich spinel formed by metasomatism and desulfurization processes at Bon Accord, South

489 Africa? Mineralogical Magazine, 78, 145–163.

490 Olsen, E. J., and Steele, I.M. (1997) Galileiite: A new meteoritic phosphate mineral. Meteoritics &

491 Planetary Science, 32, A155–A156.

492 Olsen, E.J., Kracher, A., Davis, A.M., Steele, I.A., Hutcheon, I.D., and Bunch, T.E. (1999) The

493 phosphates of IIIAB iron meteorites. Meteoritics and Planetary Science, 34, 285–300.

494 Ondruš, P., Veselovský, F., Gabašová, A., Hloušek, J., and Šrein, V. (2003) Geology and

495 hydrothermal vein system of the Jáchymov (Joachimsthal) ore district. Journal of the Czech

496 Geological Society, 48, 3–18.

497 Ouaatta, S., Assani, A., Saadi, M., and El Ammari, L. (2015) Crystal structure of strontium dinickel

498 iron orthophosphate. Acta Crystallographica, E71, 1255–1258.

499 Ouaatta, S., Assani, A., Saadi, M., and El Ammari, L. (2017) Crystal structure of calcium

500 dinickel(II) iron(III) tris(orthophosphate): $CaNi_2Fe(PO_4)_3$. Acta Crystallographica, E73, 893–

501 895.

502 Pandey, S.K., Shrivastava, J.P., and Roonwal, G.S. (2008) Occurrence of ferroan trevorite within

503 olivine megacrysts of the MORB from the Southern East Pacific Rise. Current Science, 95,

504 1468–1473.

505 Pekov, I.V., Koshlyakova, N.N., Zubkova, N.V., Lykova, I.S., Britvin, S.N., Yapaskurt, V.O.,

506 Agakhanov, A.A., Shchipalkina, N.V., Turchkova, A.G., and Sidorov, E.G. (2018) Fumarolic

507   arsenates - a special type of arsenic mineralization. European Journal of Mineralogy, 30, 305–

508   322.

509   Pérez-Cruz, M.A., Elizalde-González, M.P., Escudero, R.B., Bernès, S., Silva-González, R., and

510   Reyes-Ortega, Y. (2015) At last! The single-crystal X-ray structure of a naturally occurring

511   sample of the ilmenite-type oxide $FeCrO_3$. Acta Crystallographica, B71, 555–561.

512   Petruk, W. (1971): Mineralogical characteristics of the deposits and textures of the ore minerals. In

513   The Silver-Arsenide Deposits of the Cobalt-Gowganda Region, Ontario. Canadian

514   Mineralogist, 11, 108–139.

515   Pu, X., Rong, C., Tang, S., Wang, H., Cao, S., Ding, Y., Cao Y., and Chen, Z. (2019) Zero-strain

516    $Na_4Fe_7(PO_4)_6$ as a novel cathode material for sodium–ion batteries. Chemical

517   Communications, 55, 9043–9046.

518   Queen, W.L., Hwu, S.-J., and Wang, L. (2007) A Low-Dimensional Iron(II) Phosphate Exhibiting

519   Field-Dependent Magnetization Steps. Angewandte Chemie International Edition, 46,

520   5344−5347.

521   Roberts, A.C., Burns, P.C., Gault, R.A., Criddle, A.J., Feinglos, M.N., and Stirling, J.A.R. (2001)

522   Paganoite, $NiBiAsO_5$, a new mineral from Johanngeorgenstadt, Saxony, Germany: description

523   and crystal structure. European Journal of Mineralogy, 13, 167–175.

524   Roberts, A.C., Burns, P.C., Gault, R.A., Criddle, A.J., and Feinglos, M.N. (2004) Petewilliamsite,

525    $(Ni,Co)_{30}(As_2O_7)_{15}$, a new mineral from Johanngeorgenstadt, Saxony, Germany: description

526   and crystal structure. Mineralogical Magazine, 68, 231–240.

527   Robin, E., Bonté, P., Froget, L., Jéhanno, C., and Rocchia, R. (1992) Formation of spinels in cosmic

528   objects during atmospheric entry: A clue to the Cretaceous-Tertiary boundary event. Earth and

529   Planetary Science Letters, 108, 181–190.

530   Sharygin, V.V., Lazic, B., Armbruster, T.M., Murashko, M.N., Wirth, R., Galuskina, I.O., Galuskin,

531   E.V., Vapnik, Y., Britvin, S.N., and Logvinova, A.M. (2013): Shulamitite, $Ca_3TiFe^{3+}AlO_8$ - a

532   new perovskite-related mineral from Hatrurim Basin, Israel. European Journal of Mineralogy

533   25, 97–111.

534   Sharygin, V.V., Karmanov, N.S., and Podgornykh, N.M. (2016) Na-Fe-phosphate globules in

535   impact metal-troilite associations of Chelyabinsk meteorite. Proceeding of 79th Annual

536   Meeting of Meteoritic Society, 2016, abstract 6052.

537   Sheldrick, G.M. (2015) Crystal structure refinement with SHELXL. Acta Crystallographica, C71, 3–

538   8.

539   Smit, J. (1999) The Global Stratigraphy of the Cretaceous-Tertiary Boundary Impact Ejecta. Annual

540   Review of Earth and Planetary Science, 27, 75–113.

541   Sugiura, N., and Hoshino, H. (2003) Mn–Cr chronology of five IIIAB iron meteorites. Meteoritics

542   & Planetary Science, 38, 117–143.

543   Thorne, R.L., Roberts, S., and Herrington, R. (2012) Climate change and the formation of nickel

544   laterite deposits. Geology, 40, 331–334.

545   Vapnik, Ye., Sharygin, V., Sokol, E., and Shagam, R. (2007) Paralavas in a combustion

546   metamorphic complex, Hatrurim Basin, Israel. GSA Reviews in Engineering Geology, 18, 33–

547   153.

548   Walker, T.L. (1923) Trevorite, a distinct mineral species. Contributions to Canadian Mineralogy,

549   University of Toronto Studies, 16, 53–54.

550   White, J.S., Henderson, E.P., and Mason, B. (1967) Secondary minerals produced by weathering of

551   the Wolf Creek meteorite. American Mineralogist, 52, 1190–1197.

552   Xie, X., Chen, M., Zhai, S., and Wang, F. (2014) Eutectic metal + troilite + Fe-Mn-Na phosphate +

553   Al-free chromite assemblage in shock-produced chondritic melt of the Yanzhuang chondrite.

554   Meteoritics & Planetary Science, 49, 2290–2304.

555   Yakubovich, O.V., Mel'nikov, O.K., Urusov, V.S., Massa, V., and Vochadlo, S. (1996) Crystal

556   structure of a new orthophosphate $CsNa_3Zn_7(PO_4)_6$. Doklady Akademii Nauk SSSR, 348,

557   755−758.

558   Yakubovich, O.V., Shvanskaya, L.V., Bolotina, N.B., Ivanova, A.G., Kiriukhina, G.V., Dovgaliuk,

559   I.N., Volkov, A.S., Dimitrova, O.V., and Vasiliev, A.N. (2021) An orthorhombic modification

560   of $KCoPO_4$ stabilized under hydrothermal conditions: Crystal chemistry and magnetic

561   behavior. Inorganic Chemistry, 60, 9461–9470.

562   Zhang, H., Zhao, Y., Wen, M., Dong, Y., Fan, Q., Kuang, Q., Liu, H., and Lian, X. (2018) A new

563   sodium ferrous orthophosphate $Na_xFe_4(PO_4)_3$ as anode materials for sodium-ion batteries.

564   Journal of Materials Science, 53, 8385–8397.

565

566

567

25

568 **List of figure captions**

569 **Figure 1.** Trevorite crystal in diopside paralava. Halamish Wadi, Hatrurim Basin, Negev desert,

570 Israel. SEM BSE image. Abbreviations: Trv – trevorite; Hm – hematite; Di – diopside; Kpl –

571 keplerite $Ca_9Mg(Ca_{0.5}\square_{0.5})(PO_4)_7$

572

573 **Figure 2.** Bunsenite, NiO, in clinopyroxene-plagioclase paralava. Daba-Siwaqa complex,

574 Transjordan plateau, Jordan. (a) Bunsenite segregations (yellow) within trevorite veinlets (green)

575 that encrust the microcracks in nickeliferous hematite (blue). False colour phase distribution map

576 superimposed onto SEM BSE image. (b) The enlarged detail of the above picture, SEM BSE image.

577 Abbreviations: Bse – bunsenite; Trv – trevorite; Hem – hematite.

578

579 **Figure 3.** Yakubovichite and associated minerals. Daba-Siwaqa complex, Transjordan plateau,

580 Jordan (the type locality). (a) Yellow yakubovichite grain intergrown with brown crystals of

581 moabite $NiFe^{3+}(PO_4)O$, brownish-red crocobelonite $CaFe_2^{3+}(PO_4)_2O$ and white diopside-anorthite

582 aggregate. (b) Yellow yakubovichite grain intergrown with red crocobelonite, black areas composed

583 of hematite and Ni-phosphides, and colorless diopside. Polished thin section, transmitted light.

584 Legend: 1 – yakubovichite; 2 – moabite; 3 – crocobelonite; 4 – diopside and anorthite; 5 – hematite

585 and Ni-phosphides.

586

587 **Figure 4.** Crystal structure of yakubovichite (α-$CrPO_4$ structure type). A three-dimensional

588 framework consisting of corner- and edge-sharing [MO_6] octahedra and [PO_4] tetrahedra. The

589 framework is penetrated by the two systems of channels: (a) the channels propagated along the *a*-

590 axis and (b) those propagated along the *b*-axis. Alkali earth and alkali cations (not shown for clarity)

591 reside in the channels. Blue tetrahedra, [PO_4]; yellow octahedra, [$M1O_6$]; green octahedra, [$M2O_6$].

26

592

593   **Figure 5.** Raman spectrum of yakubovichite. (a) The fingerprint region. (b) Region 1350-3800 cm^{-1}.

594   The intensity scale in (a) and (b) is the same.

595

596   **Figure 6.** Stratigraphic position of pyrometamorphic lithologies of the Hatrurim Basin, Israel, and

597   the coincident lithologies of the Daba-Siwaqa complex, Jordan, in the Late Cretaceous–Paleogene

598   sequence of the Southern Levant. The stratigraphic equivalents of the Mottled Zone are highlighted

599   by brown color. The Cretaceous-Paleogene boundary (~66 Ma) is marked by the red line. Redrawn

600   based on the data of Britvin et al. (2021c).

601

602

603

604

605 **Table 1**. Chemical composition of Ni-bearing oxides (wt.%) from the Hatrurim Formation [a]

606

Mineral	Trevorite				Bunsenite		Eskolaite	Hematite		
Locality	HB [b]	DS [b]	HB	DS	DS		DS	HB	DS	DS
Notes	Fig. 1			Fig. 2	Fig. 2					Fig. 2
NiO	29.93	30.15	29.23	29.24	89.73	90.11	1.83	1.25	2.38	1.73
CoO	0.53							0.23		
FeO					6.85	8.91				
CaO	0.41		0.35	0.48			0.51	0.40		0.57
CuO	1.36	1.64	1.18					0.17		
Al_2O_3	1.00	13.07	0.96	0.90	3.16	1.25	3.07			2.81
V_2O_3							2.59	0.69		
Cr_2O_3	1.60		2.75				55.42	0.34		2.36
Fe_2O_3	65.80	56.19	65.37	70.34			35.45	96.35	97.94	90.53
TiO_2							1.60	1.15		1.85
SiO_2					0.37	0.15				1.12
Total	100.63	101.05	99.84	100.96	100.11	100.42	100.47	100.58	100.32	100.97
Formula amounts (*apfu*) (based on the number of oxygen atoms given in the bottom line)										
Ni	0.93	0.87	0.91	0.90	0.86	0.88	0.04	0.03	0.05	0.04
Co^{2+}	0.02									
Fe^{2+}					0.07	0.09				
Ca	0.02		0.01	0.02			0.01	0.01		0.02
Cu^{2+}	0.04	0.04	0.03							
Al	0.05	0.55	0.04	0.04	0.04	0.02	0.09			0.08
V^{3+}							0.05	0.01		
Cr^{3+}	0.05		0.08				1.11	0.01		0.05
Fe^{3+}	1.91	1.51	1.90	2.02			0.67	1.92	1.97	1.75
Ti^{3+}							0.04	0.03		0.04
Si										0.03
Σ	3.02	2.97	2.97	2.98	0.97	0.99	2.01	2.01	2.02	2.01
O	4	4	4	4	1	1	3	3	3	3

607

608 [a] Blank cells denote that element contents are below detection limit (<0.05 wt.%). [b] Locality

609 abbreviations: HB – Hatrurim Basin, Negev desert, Israel; DS – Daba-Siwaqa complex, Jordan.

610

611

28

612

613 **Table 2**. Chemical composition of yakubovichite [a]

614

Locality	Daba-Siwaqa, Jordan (holotype)			Hatrurim Basin, Israel		
	$n = 7$	range	s.d.	$n = 8$	range	s.d.
Na_2O	1.82	1.35 – 2.18	0.28	1.49	1.30 – 1.75	0.15
K_2O	1.76	1.63 – 2.00	0.16	1.04	0.91 – 1.23	0.11
CaO	6.37	6.07 – 6.88	0.32	7.23	6.74 – 7.91	0.43
SrO	0.49	0.26 – 0.69	0.18	0.39	0.27 – 0.57	0.14
BaO	1.37	1.07 – 1.65	0.20	2.37	2.03 – 2.81	0.31
MgO	2.13	1.24 – 2.88	0.52	3.40	2.93 – 4.11	0.41
CoO				0.06	0.00 – 0.27	0.12
NiO	21.39	20.38 – 22.49	0.68	19.96	18.83 – 21.09	0.68
CuO	0.16	0.00 – 0.37	0.13	0.22	0.00 – 0.48	0.19
Fe_2O_3	18.80	17.76 – 19.45	0.60	18.14	17.2 – 18.95	0.59
Al_2O_3	1.06	0.78 – 1.44	0.23	0.68	0.35 – 0.97	0.19
V_2O_3	0.44	0.26 – 0.71	0.16	0.87	0.44 – 1.47	0.33
Cr_2O_3	0.15	0.00 – 0.49	0.18	0.11	0.00 – 0.17	0.07
SiO_2				0.22	0.00 – 0.42	0.17
TiO_2				0.08	0.00 – 0.26	0.11
P_2O_5	44.15	43.49 – 44.73	0.38	43.85	42.75 – 44.55	0.57
Total	100.09			100.11		

615

616   [a] Blank cells denote that element contents are below detection limit (<0.05 wt.%).

617

618

619

29

620

621   **Table 3.** Scattering factors, site occupancies and bond-valence sums (*v.u.*) for cation sites of
622   yakubovichite from the Daba-Siwaqa complex, Jordan (the holotype)

623

Site	SC [a]	SOF [b]	SSF [c]	Assigned site occupancy	Site charge	Z [d]	BVS [e]
A	Ca, Na	$Ca_{0.78}Na_{0.22}$	18.02	$Ca_{0.51}Na_{0.29}K_{0.18}Ba_{0.04}Sr_{0.02}$	1.56	19.08	1.26
$M1$	Fe, Al	$Fe_{0.90}Al_{0.10}$	24.70	$Fe^{3+}_{0.90}Al_{0.10}$	3.00	24.70	3.07
$M2$	Ni, Mg	$Ni_{0.90}Mg_{0.10}$	26.40	$Ni_{0.72}Mg_{0.13}Fe^{3+}_{0.12}V^{3+}_{0.02}Cu^{2+}_{0.01}$	2.14	25.52	2.11

624

625   [a] SC, atomic scattering curves used for site occupancy refinement. [b] SOF, refined site occupancy factor. [c]
626   SSF, refined site-scattering factor (number of electrons per site). [d]Z, mean site atomic number calculated from
627   electron microprobe data, normalized to site population = 1. Bond-valence coefficients from Brese and
628   O'Keeffe (1991).
629

630 **Table 4.** Crystal parameters of yakubovichite, its synthetic analogue and related phosphates
631

	Yakubovichite	**Synthetic**	**Synthetic**	**Xenophyllite**	**Synthetic** [a]
Formula	$CaNi_2Fe^{3+}(PO_4)_3$	$CaNi_2Fe^{3+}(PO_4)_3$	$SrNi_2Fe^{3+}(PO_4)_3$	$Na_4Fe_7(PO_4)_6$	$Na_{1.1}Fe_4(PO_4)_3$
Crystal system	Orthorhombic	Orthorhombic	Orthorhombic	Orthorhombic [b]	Monoclinic
Space group	*Imma*	*Imma*	*Imma*	*Imma* or *Im2a* [b]	*P*2$_1$/*n*
a (Å)	10.388	10.313	10.388	10.298	6.369
b (Å)	13.088	13.114	13.159	14.997	9.950 [c]
c (Å)	6.479	6.441	6.512	6.351	15.666
V (Å^3)	880.94	871.0	890.2	981.0	992.3
Z	4	4	4	2	4
Reference	This paper	Ouaatta et al. (2017)	Ouaatta et al. (2015)	Britvin et al. (2020)	Zhang et al. (2018)

632

633 [a] A likely synthetic analogue of galileiite, NaFe$_4$(PO$_4$)$_3$. [b] Body-centered subcell (Britvin et al.
634 2020d). [c] β = 91.9°.

635

636
637
638

639 **Table 5**. X-ray powder diffraction data (d in Å) for holotype yakubovichite [a]

I_{meas}	d_{meas}	I_{calc}	d_{calc}	hkl	I_{meas}	d_{meas}	I_{calc}	d_{calc}	hkl
5	6.57	2	6.54	020	1	1.813	1	1.814	233
44	5.82	32	5.81	011	14	1.774	4	1.775	361
73	5.51	51	5.50	101			19	1.773	451
32	5.21	33	5.19	200	4	1.757	6	1.755	352
34	4.214	23	4.209	121	2	1.734	3	1.733	512
24	4.075	19	4.068	220	25	1.723	34	1.723	442
13	3.874	16	3.871	211	1	1.695	1	1.698	271
9	3.616	4	3.619	031			2	1.693	541
20	3.239	15	3.240	002	5	1.664	9	1.666	053
20	3.057	18	3.054	301	3	1.637	11	1.636	080
31	3.013	14	3.010	112	4	1.618	7	1.620	004
12	2.889	4	2.903	022	3	1.599	2	1.600	172
9	2.818	7	2.812	141	9	1.586	13	1.586	253
97	2.772	100	2.768	240	3	1.571	3	1.572	024
100	2.748	83	2.749	202	4	1.544	5	1.546	204
38	2.599	41	2.597	400	11	1.528	12	1.530	640
12	2.527	6	2.534	222			12	1.527	602
		8	2.523	132	1	1.484	2	1.485	462
3	2.431	5	2.427	051	1	1.444	3	1.447	701
3	2.231	1.4	2.233	341			1	1.442	381
17	2.201	24	2.199	251	2	1.420	5	1.419	091
18	2.129	16	2.131	013	3	1.409	7	1.410	651
9	2.080	7	2.080	332	7	1.402	14	1.402	453
12	2.033	13	2.034	440	2	1.371	6	1.369	291
7	1.998	6	1.998	152	1	1.362	1	1.362	543
5	1.971	4	1.972	213	2	1.344	3	1.345	424
1	1.893	2	1.894	521	3	1.298	7	1.298	800
6	1.831	6	1.832	303	4	1.266	6	1.267	444

640
641 [a] Calculated lines with intensity less than 1 have been omitted.

642
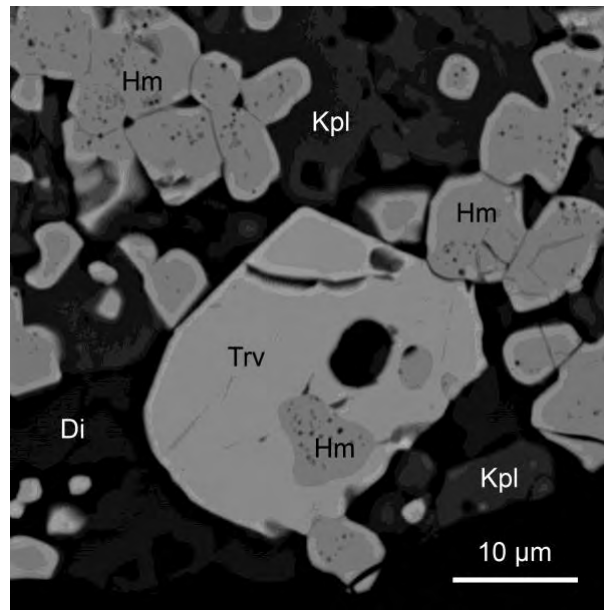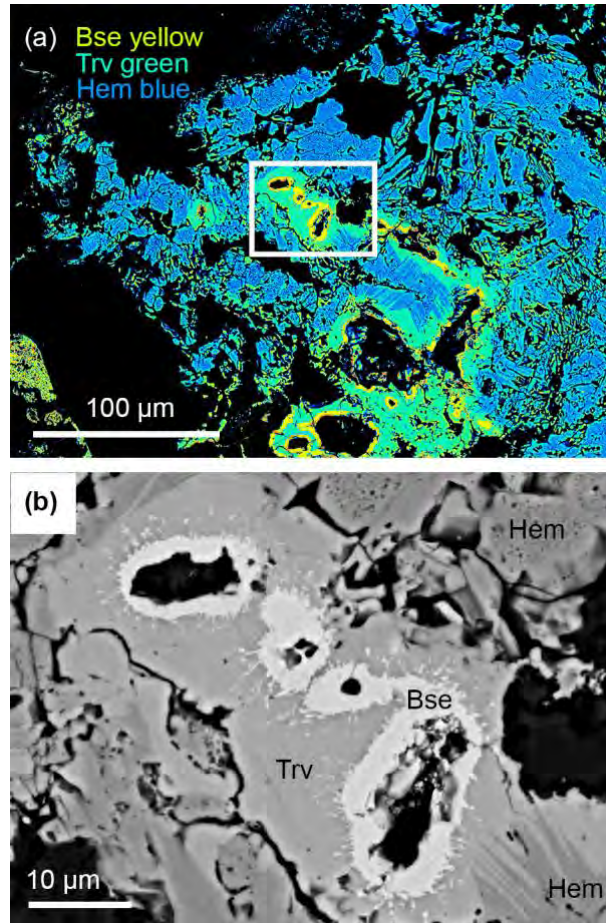
643

32

644

645

646 **Figure 1.**

647

648

649

650

651 **Figure 2.**

652

653

34

654

655

656

Figure 3.

657

658

659

660   **Figure 4.**

661

662

663

664

665

Figure 5.

666
667
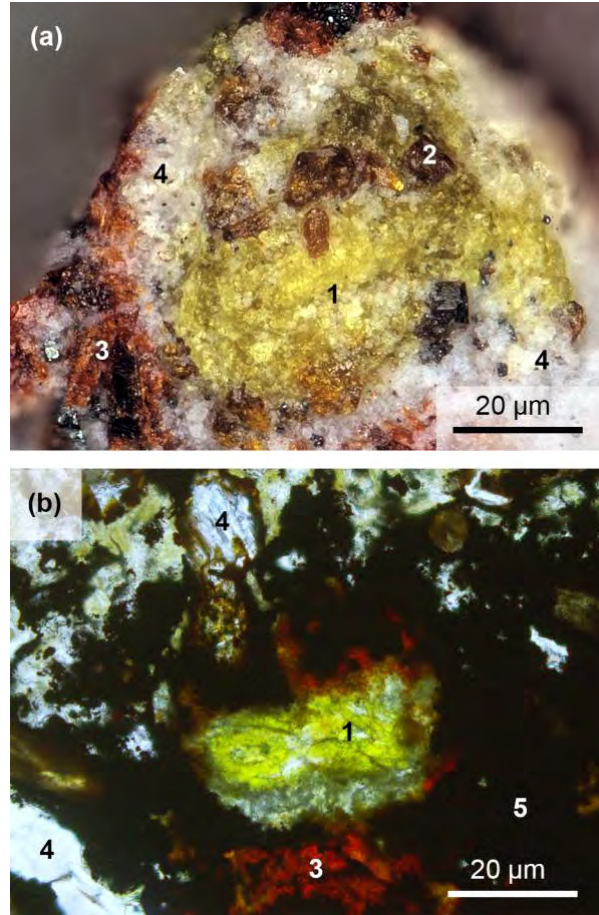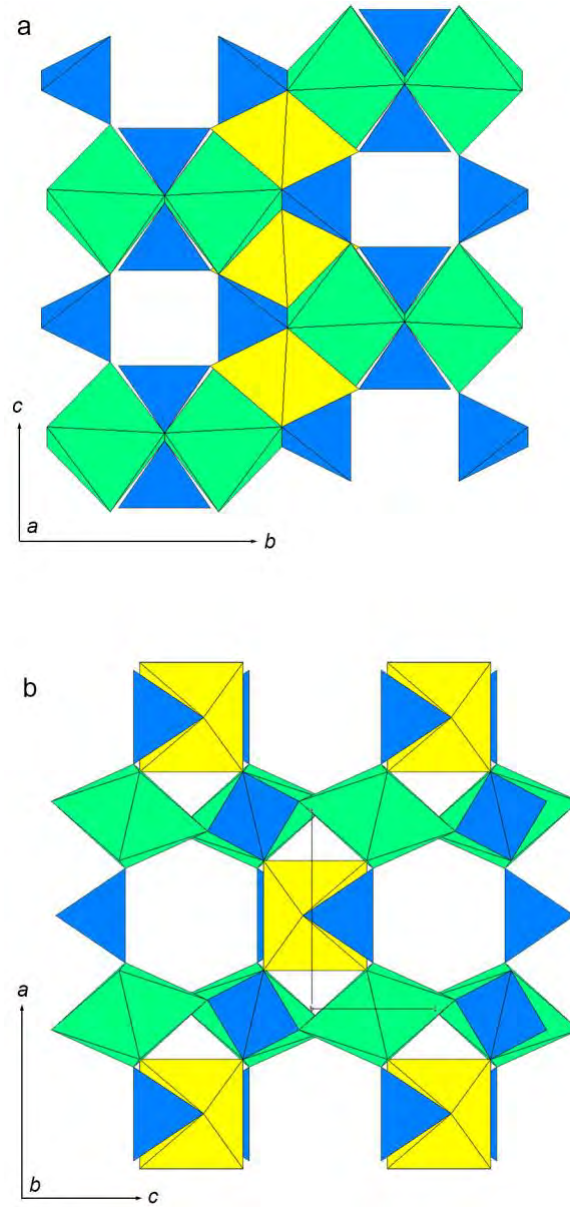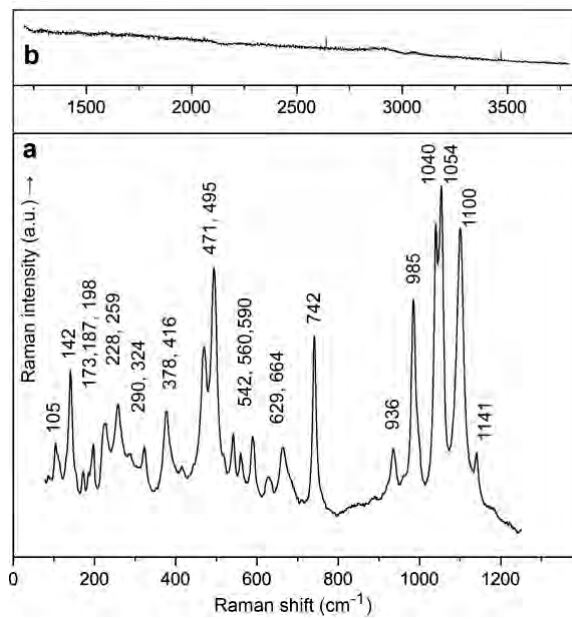
668

669

	Age	Israel		Jordan	
		Formation, thickness (m)	Normal facies	Formation, thickness (m)	Normal facies
Paleogene	Eocene			Umm Rijam (45)	Chert Marl Chalk
	Paleocene	Taqiye (30)	Chalk Marl	Muwwaqqar (150)	Marl Limestone
	— 66 Ma —				
	Maastrichtian	Ghareb (70)	Chalk		
Late Cretaceous	Campanian	Mishash (80)	Phosphorite Chalk Chert	Al Hisa (70)	Phosphorite Limestone Chert
	Santonian	Menuha (50)	Chalk	Wadi Umm Ghudran (40)	Chalk Limestone
	Coniacian			Wadi As Sir (120)	Limestone Dolomite Marl
	Turonian	Bina (70)	Limestone Dolomite		

670

671 **Figure 6.**
672